

Journal of Materials Chemistry A

Accepted Manuscript



This is an *Accepted Manuscript*, which has been through the Royal Society of Chemistry peer review process and has been accepted for publication.

Accepted Manuscripts are published online shortly after acceptance, before technical editing, formatting and proof reading. Using this free service, authors can make their results available to the community, in citable form, before we publish the edited article. We will replace this *Accepted Manuscript* with the edited and formatted *Advance Article* as soon as it is available.

You can find more information about *Accepted Manuscripts* in the [Information for Authors](#).

Please note that technical editing may introduce minor changes to the text and/or graphics, which may alter content. The journal's standard [Terms & Conditions](#) and the [Ethical guidelines](#) still apply. In no event shall the Royal Society of Chemistry be held responsible for any errors or omissions in this *Accepted Manuscript* or any consequences arising from the use of any information it contains.

Tunable mesoporous manganese oxide for high performance oxygen reduction and evolution reactions[§]

Islam M. Mosa^{1,2†}, Sourav Biswas^{1†}, Abdelhamid M. El-Sawy^{1,2}, Venkatesh Botu⁴, Curtis Guild¹, Wenqiao Song¹, Rampi Ramprasad⁴, James Rusling^{1,3,5}, Steven L. Suib^{1,6*}

¹Department of Chemistry, University of Connecticut, 55 North Eagleville Road, Storrs, Connecticut 06269, United States

²Department of Chemistry, Tanta University, Tanta 31527, Egypt

³Department of Cell Biology, University of Connecticut Health Center, Farmington, Connecticut 06032, United States

⁴University of Connecticut, Chemical and Biomolecular Engineering, 97 North Eagleville Road, Unit 3136, Storrs, Connecticut 06269, United States

⁵School of Chemistry, National University of Ireland, Galway, University Road, Galway, Ireland

⁶Institute of Materials Science, University of Connecticut, U-3060, 55 North Eagleville Rd., Storrs, Connecticut 06269, United States

† I.M and S.B contributed equally

[§]Electronic supplementary information (ESI) available: List of chemicals, SEM images, more characterizations of ORR and OER, XPS, XANES, EXAFS, TR-PXRD, CO₂ adsorption, additional DFT data and comparison between various manganese oxide catalysts from the literature.

Abstract:

Understanding the origin of manganese oxide activity for oxygen reduction reaction (ORR) and oxygen evolution reaction (OER) is a key step towards rationally designing of highly active catalysts capable of competing with the widely used, state-of-art noble metal catalysts. Herein, we present a bifunctional, thermally stable cesium-promoted mesoporous manganese oxide (Cs-MnOx) tuned by simple heat treatment from an amorphous to a crystalline phase with controlled surface and bulk active Mn centers. The Cs-MnOx material exhibited the highest ORR activity (0.87 V vs. RHE at -3 mA/cm²) among all noble-metal-free manganese oxide catalysts reported to date with superior activity compared to state-of-the-art Pt/C catalyst. In addition, Cs-MnOx exhibited comparable OER performance with the highly active Ir/C and RuO₂ catalysts. Extensive characterization and density functional theory (DFT) computations suggested that the stabilization of the surface and bulk enriched Mn³⁺ species, increase of relative basicity and maintaining active crystalline phase due to Cs incorporation, are the main decisive factors for the profound ORR and OER activities. Findings from our study provide general guidance for designing of cost effective and active metal oxide based electrocatalysts.

Introduction:

Recent and impending global energy crises have stimulated extensive research efforts in renewable energy production and storage.^{1,2} In particular, the oxygen reduction reaction (ORR) and oxygen evolution reaction (OER) are of great interest due to their importance with respect to a number of energy conversion applications, including fuel cells and water splitting systems.^{3,4} Bifunctional OER and ORR catalysts are of special significance for energy storage in rechargeable metal-air batteries, where both reactions happen at the cathode during charging and discharging processes.⁵ One of the difficulties associated with ORR and OER is their sluggish reaction kinetics, which results in low system efficiency. Precious metals like platinum (for ORR) and oxides of iridium or ruthenium (for OER) are considered state-of-art catalysts achieving very high catalytic activity.⁶⁻⁸ The high cost, scarcity, and relatively low stability of precious metals for ORR and OER have resulted in great interest in the development of alternative bifunctional electrocatalysts that are efficient, cost-effective and robust.^{9,10}

Among non-precious metal oxides, manganese oxides are especially attractive as electrocatalysts due to their natural abundance, low toxicity, multivalent nature and structural diversity (more than 30 crystal structures corresponding to different polymorphs are known to exist).¹¹ Manganese oxides have also inspired great interest as catalysts for water oxidation due to the natural presence of the highly OER active CaMn_4O_x cluster in the oxygen evolving complex (OEC) of Photosystem II involved in photosynthesis.¹²⁻¹⁴ Several types of manganese oxide catalysts (rutile, spinel, peroxide, tunnel, birnessite) have been used as water oxidation and oxygen reduction catalysts in alkaline media.¹⁵⁻¹⁹ However, the documented ORR and OER activities are still low compared with the state-of-art Pt-, Ru-, or Ir-based catalysts which hinder their use in real-world applications. Extensive studies have been made on the structure-property relationship of different Mn oxides with the aim of enhancing their catalytic activity.^{20,21}

The rational design of active ORR and OER manganese oxide catalysts require choosing the active manganese oxide phase (crystalline or amorphous), active Mn oxidation state, optimization of surface and

bulk Mn centers, as well as high surface area. Towards that end, researchers have used mesoporous materials as active electrocatalysts due to their high surface area, and tunable porous structure.²²⁻²⁴ Attempts have been made to tune the Mn oxidation state by introducing different elements to manganese oxide catalysts. Incorporation of Au nanoparticles in Mn oxide was found to promote the formation of surface-active Mn^{3+} species, which resulted in a significant enhancement in water oxidation activity over typical Mn oxides^{25, 26}. Alkaline earth metals are also known to influence the catalytic activity of manganese oxides²⁷.

Herein, we document a bifunctional Cs ion-promoted mesoporous manganese oxide (Cs-MnO_x) synthesized by a facile soft-templated inverse micelle approach for ORR and OER.^{28, 29} The material exhibited aggregated nanocrystalline nature with tunable mesoporous size. Simple heat treatment of Cs-MnO_x enabled precise control over surface and bulk active Mn^{3+} species, pore size, surface area, and crystallinity, making this mesoporous material well-suited for investigating the origin of manganese oxide activity for ORR and OER. Cs-MnO_x calcined at 450 °C (Cs-MnO_x -450) outperformed other reported noble-metal free manganese oxide catalysts for ORR and also exhibited a very high activity in OER, achieving the smallest difference in potential between ORR (at -3 mA/cm²) and OER (at 10 mA/cm²) among all manganese oxide catalysts reported (0.78 V). Moreover, the ORR activity of Cs-MnO_x -450 was higher than the state-of-art Pt/C catalysts with faster electron transfer rate. In the case of OER, the activity was lower than the highly active Ir/C and RuO_2 catalysts at low current density, but higher at high current density with 4 fold higher stability. Physical and electrochemical studies supported by theoretical validation confirmed the critical roles of surface and bulk-enriched Mn^{3+} , stabilization of active crystalline phase, and high surface area in the superior electrocatalytic behavior of Cs-MnO_x .

Results

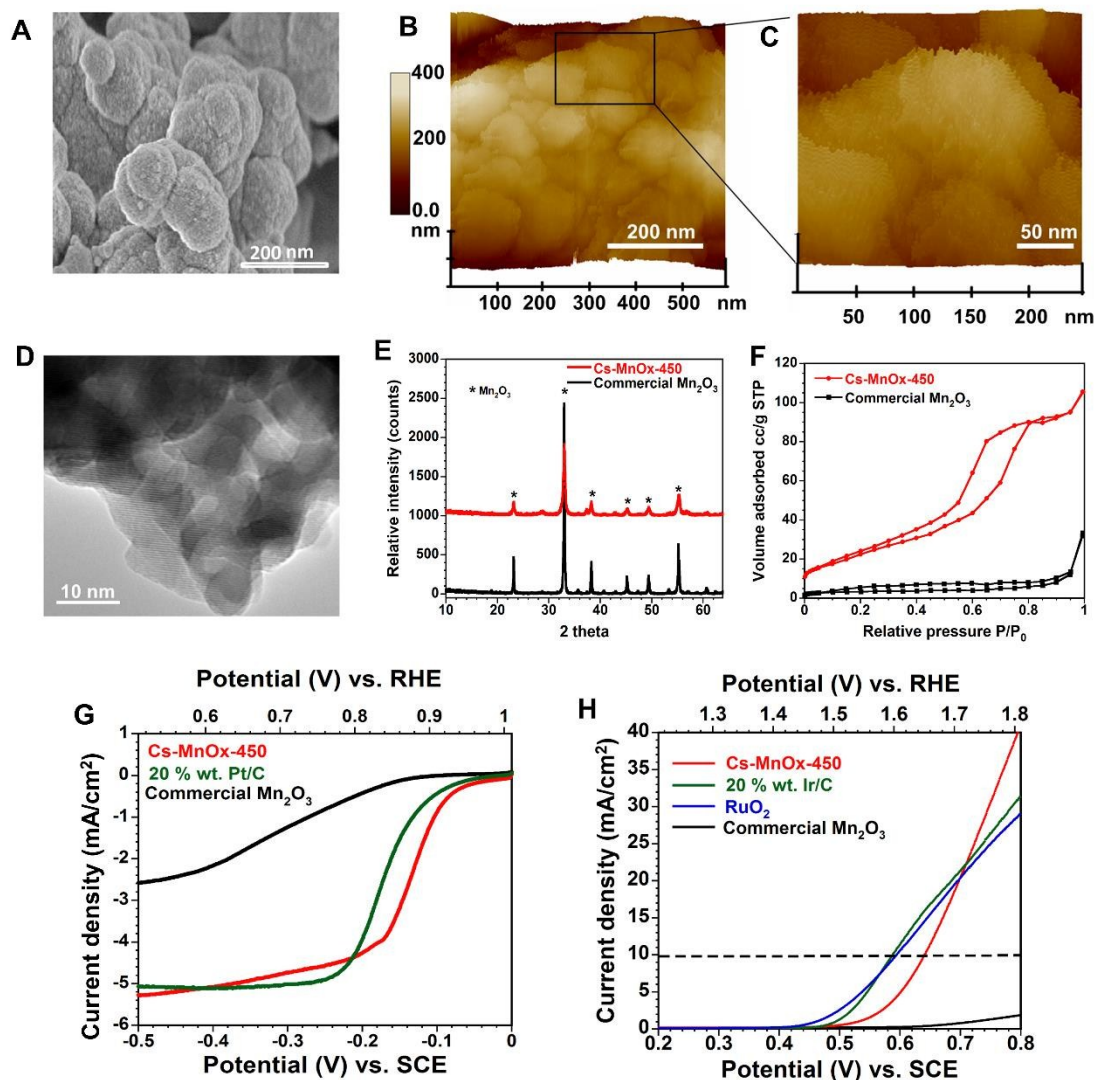


Fig. 1 Comparison of the best optimized Cs-MnO_x-450 to commercial and state-of-art catalysts. (A) FE-SEM. (B) AFM with magnification in (C) showing a mean surface roughness (R_a) of 22 ± 3 nm. R_a is defined as the average surface height deviations measured from the mean plane within a selected area of $1 \mu\text{m}^2$. (D) TEM image showing the lattice distances of 0.27 nm which are indexed to bixbyite Mn₂O₃ (222) planes. (E) PXRD, (F) N₂ sorption, (G) Linear sweep voltammetry (LSV) curves for ORR, and (H) LSV curves for OER.

The physicochemical and morphological features of Cs-MnO_x catalysts were extensively characterized by powder X-ray diffraction (PXRD), N₂ sorption, scanning electron microscopy (SEM), X-ray photoelectron spectroscopy (XPS), X-ray absorption near-edge spectra (XANES), extended X-ray absorption fine structure (EXAFS), transmission electron microscopy (TEM), atomic force microscopy (AFM) and inductive coupled plasma - mass spectrometry (ICP-MS). The morphology of the Cs-MnO_x material calcined at 450 °C (highest activity for ORR and OER among all calcination temperatures) was investigated using SEM, TEM, and AFM (**Fig. 1A-D**). The field-emission scanning electron microscopy (FE-SEM) image of Cs-MnO_x-450 (**Fig. 1A, and S1**) showed aggregated round shaped nanoparticles. Tapping mode AFM was used for exploring the surface of the Cs-MnO_x-450, and the surface roughness was analyzed to be 22 ± 3 nm, providing a nearly uniform rough catalytic surface for the reactions (**Fig. 1B-C**). The TEM image of Cs-MnO_x-450 revealed the crystalline nature of the material with a measured lattice spacing of 0.27 nm that was assigned to the (222) planes of Mn₂O₃ (bixbyite) phase (**Fig. 1D**). **Fig. 1E** showed the wide angle (5° - 75°) powder X-ray diffraction (PXRD) patterns of Cs-MnO_x-450 and commercial Mn₂O₃, which confirmed the crystalline Mn₂O₃ (bixbyite) phase of Cs-MnO_x. In addition, the Cs-MnO_x-450 material possessed a Type IV adsorption isotherm followed by a hysteresis loop (indication of regular mesoporous structure) as obtained by the N₂ sorption measurements, whereas the isotherm nature of commercial Mn₂O₃ confirmed the nonporous structure. (**Fig. 1F**). The exceptional electrochemical properties of mesoporous Cs-MnO_x-450 compare to commercial Mn₂O₃, Pt/C, Ir/C and RuO₂ towards ORR and OER are shown in **Fig. 1G-H**. The mesoporous Cs-MnO_x-450 displayed much higher activity compared to the commercial nonporous Mn₂O₃. Moreover, the ORR performance of the Cs-MnO_x-450 outperformed the state-of-art Pt/C catalyst with 30 mV more positive potential at -3 mA/cm² (**Fig. 1G**). On the other hand, the OER behavior of the Mn₂O₃ showed lower activity as compared to the highly active Ir/C and RuO₂ catalysts at low current density, but higher activity at high current density (**Fig. 1H**).

In order to further understand the origin of the ORR and OER activity, the Cs-MnO_x was calcined at different temperatures, and the changes in the chemical and electrochemical properties were investigated.

The material transformed from amorphous ($< 450\text{ }^{\circ}\text{C}$) to crystalline Mn_2O_3 (bixbyite) phase ($\geq 450\text{ }^{\circ}\text{C}$) with the heat treatment as evidenced by wide-angle PXRD patterns (Fig. 2A). No other intermediate phases of Mn and Cs were observed in the PXRD. Cs-MnO_x materials possessed a Type IV adsorption isotherm regardless of the heat treatment up to $550\text{ }^{\circ}\text{C}$, indicating regular mesoporous structure, while increasing the temperature to $650\text{ }^{\circ}\text{C}$ led to destruction of mesoporous structure (Fig. 2B). The Brunauer–Emmett–Teller (BET) method was used to calculate surface areas of the different Cs-MnO_x materials (Table 1). Of the different Cs-MnO_x materials prepared by controlling calcination temperature, Cs-MnO_x-350 exhibited the maximum surface area ($106\text{ m}^2/\text{g}$) while Cs-MnO_x-450 possessed the largest surface area ($86\text{ m}^2/\text{g}$) for crystalline Cs-MnO_x materials. The Cs-MnO_x materials showed monomodal uniform pore size distributions upto calcination temperature $550\text{ }^{\circ}\text{C}$ (Fig. 2C). As calculated by the Barrett-Joyner-Halenda (BJH) method, pore size increased from 3.4 to 7.8 nm with the calcination temperature from $250\text{ }^{\circ}\text{C}$ to $550\text{ }^{\circ}\text{C}$ (Fig. 2C, and Table S1). The pore size increment can be attributed to the interaction of nanoparticles to form bigger size nanoparticles, thus increasing the corresponding intraparticle voids.²⁹ Nanoparticle interaction and aggregation can also explain the reduction of surface area of catalysts heated at high temperatures. Though mesoporosity of the material was well preserved up to $550\text{ }^{\circ}\text{C}$, the material calcined at $650\text{ }^{\circ}\text{C}$ exhibited very low surface area ($13\text{ m}^2/\text{g}$) with loss of mesoporosity (no Type IV adsorption isotherm, see Fig. 2B).

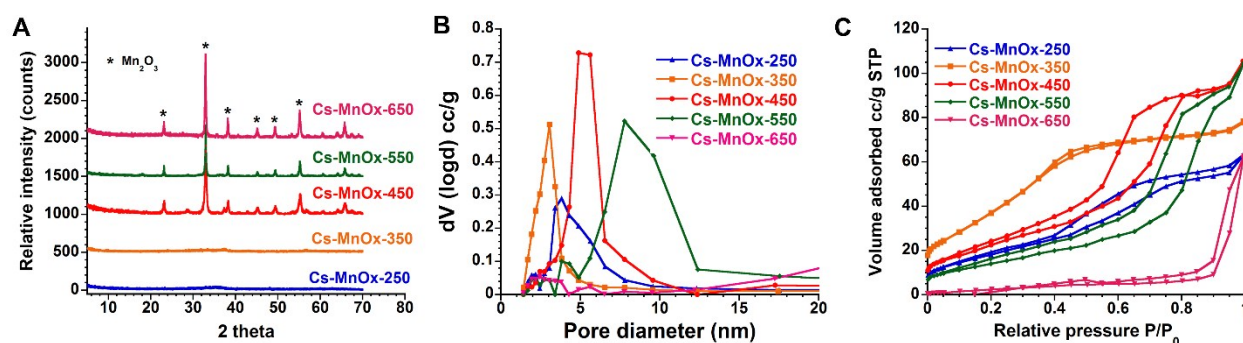


Fig. 2 Structural characterization of Cs-MnO_x calcined at different temperatures. (A) PXRD patterns, (B) N₂ adsorption-desorption isotherms, and (C) BJH desorption pore size distribution.

Oxygen reduction reaction

In order to evaluate the electrocatalytic performance of the aforementioned materials, catalyst ink was prepared and loaded onto the pyrolytic graphite electrodes (0.28 mg/cm² mass loading for all catalysts). Linear sweep voltammetry (LSV) was tested in 0.1 M KOH solution using a rotating disc electrode (see experimental section for detailed experimental conditions). LSV polarization curves displayed slight enhancement in ORR activity of the Cs-MnO_x upon increasing the calcination temperature from 250 °C to 350 °C, however the current was still low compared to the Pt/C catalyst (**Fig. 3A, Table 1**). Upon increasing the calcination temperature from 350 °C to 450 °C, a dramatic enhancement in the ORR activity was observed with 230 mV positive shift of potential at -3mA/cm² and significant increase in ORR current. By further increasing the calcination temperature above 450 °C, a sharp reduction in ORR activity was observed (**Fig. 3A, Table 1**). The material calcined at 450 °C displayed the highest activity among all calcination temperatures, with superior activity compared to Pt/C and the non-promoted manganese oxide calcined at 450 °C (MnO_x-450) (**Table 1**). At a current density of -3 mA/cm², Cs-MnO_x-450 showed a potential of -0.14 V vs. SCE (0.87 V vs. RHE), which is 30 mV more positive as compared to 20 % wt. Pt/C catalyst and 230 mV more positive as compared to the corresponding non-promoted mesoporous manganese oxide (**Fig. 3A**). For further characterization of the ORR behavior of the most active material Cs-MnO_x-450, cyclic voltammetry (CV) was tested in both argon and oxygen saturated 0.1 M KOH. The CV curves showed no observable ORR behavior in Ar saturated KOH, while a well-defined reduction peak was observed in oxygen saturated KOH (**Fig. 3B**). Moreover, the highest active Cs-MnO_x material calcined at 450 °C presented a Tafel slope (69 mV/dec) smaller than that of Pt/C (89 mV/dec) (**Fig. 3F, and Table 1**).

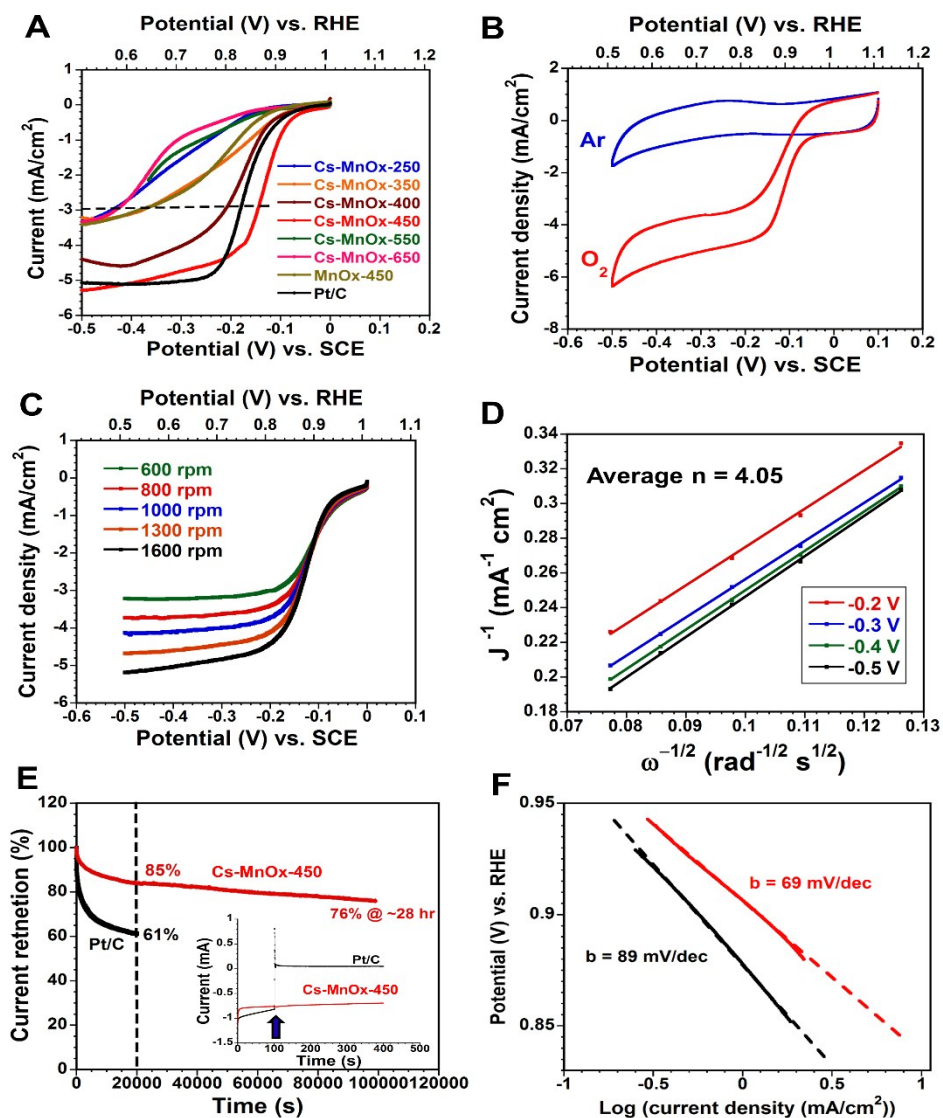


Fig. 3 ORR performance of the different catalysts in 0.1 M KOH. (A) LSV polarization curves at a scan rate of 5 mV/s and rotation speed of 1600 rpm. (B) CV curves at 25 mV/s for the best optimized Cs-MnO_x-450 catalyst in both O₂ and Ar saturated 0.1 M KOH. (C) LSV curves of the Cs-MnO_x-450 at different rotation speeds. (B) The corresponding Koutecky–Levich plots for Cs-MnO_x-450 at different potentials from -0.2 to -0.5 vs. SCE (0.81-0.51 V vs. RHE). (E) *i-t* chronoamperometric responses for Cs-MnO_x-450 compared to Pt/C at -0.3 V vs. SCE (0.71 V vs. RHE), with inset showing the effect of methanol addition (blue arrow) on the ORR performance. (F) Tafel plots for the ORR of Cs-MnO_x-450 (red color) as compared to Pt/C (black color).

Table 1: Summary for the structural parameters and ORR performance for the studied catalysts.

Sample ID	Crystal structure ^a	Surface area (m ² /g) ^b	ORR E _j (V) @ -3 mA/cm ² ^c	R _{ct} (Ω) ^d	k ^o (cm s ⁻¹) ^e
Cs-MnO _x -250	Amorphous	79	-0.43 (0.58)	850	0.0004
Cs-MnO _x -350	Amorphous	106	-0.37 (0.64)	550	0.0006
Cs-MnO _x -450	Mn ₂ O ₃ (bixbyite)	86	-0.14 (0.87)	105	0.0032
Cs-MnO _x -550	Mn ₂ O ₃ (bixbyite)	53	-0.43 (0.58)	858	0.0004
Cs-MnO _x -650	Mn ₂ O ₃ (bixbyite)	13	-0.43 (0.58)	1550	0.0002
MnO _x -450	Mn ₂ O ₃ (bixbyite)	150	-0.37 (0.64)	559	0.0006
20 % wt. Pt/C	N/A	N/A	-0.17 (0.84)	207	0.0016

^aObtained from PXRD. ^bDetermined by BET method. ^cThe potential for ORR measured at a current density of -3 mA/cm² in 0.1 M KOH as extracted from LSV, Potentials are recorded in volts versus SCE, and converted to RHE in parentheses. ^dThe charge transfer resistance (R_{ct}) obtained from EIS analysis at a potential of -0.15 V vs. SCE (0.86 vs. RHE). ^eThe standard rate constant calculated from R_{ct} values (see calculation formulas in the methodology section). N/A stands for not applicable.

To investigate reaction kinetics, electrochemical impedance spectroscopy (**Fig. S2**) was performed, and the charge transfer resistance (R_{ct}) was obtained (**Table 1**) from the fitted equivalent circuit (using Zimo V3.5 software). The R_{ct} (as determined from the diameter of the semicircle of the Nyquist plot at high frequency region) was used to calculate the exchange current density (*J*_o) and the standard rate constant (k^o) as two important kinetic parameters for comparing electron transfer rates (R_{ct} is inversely proportional to both *J*_o and k^o, see equations in experimental section). The highest active Cs-MnO_x-450 showed the smallest R_{ct} (105 Ω) among all studied catalysts, a little more than half that of the Pt/C (207 Ω) at a constant potential of -0.15 V vs. SCE (0.86 V vs. RHE). Therefore, Cs-MnO_x-450 has the highest *J*_o and k^o among studied catalysts with ~ two fold faster electron transfer rate compared to Pt/C (**Table 1, and Table S2**). The R_{ct}

values were strongly correlated to the activities presented by LSVs in **Fig. 3A**. More insights on the ORR kinetics of Cs-MnO_x-450 were evaluated by rotating disc electrode experiments at different rotation speeds (**Fig. 3C**). The linearity and nearly parallel lines of the Koutecky-Levich plots (**Fig. 3D**) indicated a first order reaction with respect to the concentration of dissolved oxygen in a four electron transfer process at a wide potential range (-0.2 to -0.5 V vs. SCE, 0.81 to 0.51 V vs. RHE) (**Fig. S3**).

The stability of the Cs-MnO_x-450 in comparison with Pt/C was tested at a constant potential of -0.3 V vs. SCE (0.71 V vs. RHE) using chronoamperometric current-time (i-t) curves (**Fig. 3E**). The Pt/C catalyst lost 39% of its initial activity after 5.5 h, while Cs-MnO_x-450 displayed much higher stability with a loss of only 15% of its initial activity after 5.5 h and 23% after ~ 28 h. Methanol tolerance is a critical feature for the cathode material used in proton exchange membrane fuel cells (PEMFCs), specifically in direct-methanol fuel cells.³⁰ Addition of methanol to the ORR chronoamperometric experiment of the Pt/C electrocatalyst resulted in a complete loss of the ORR activity due to the methanol oxidation by the Pt/C catalyst.³¹ In contrast, Cs-MnO_x-450 exhibited very high methanol tolerance (inset of **Fig. 3E**). These results signified the robustness of Cs-MnO_x-450 as ORR catalyst for direct-methanol fuel cell as well as alkaline fuel cells.

Oxygen evolution reaction

In addition to ORR, we examined the bifunctionality of the Cs-MnO_x material by testing the OER performance as well. The OER performance of Cs-MnO_x was evaluated at different calcination temperatures and compared to the highly OER active Ir/C and RuO₂ catalysts. Similar to ORR, significant variations in OER activity were observed by changing the calcination temperatures of the Cs-MnO_x. LSV polarization curves displayed slight enhancement in OER activity when the calcination temperature increased from 250 °C to 350 °C followed by a dramatic enhancement in activity when the calcination temperature increased from 350 °C to 450 °C as shown by the enhancement in current and the shift of onset potential to a less positive potential. Significant decrease in the activity was then noted when the calcination

temperature increased to 550 °C and 650 °C (Fig. 4A, Table 2). The charge transfer resistance obtained from the fitted data circuit of the EIS spectra at 0.7 V vs SCE. (1.71 V vs. RHE) confirmed the same trend seen in LSVs. The smallest R_{ct} of all calcination temperatures of Cs-MnO_x was recorded for Cs-MnO_x-450 (50 Ω), which is close to that of the highly active Ir/C (37 Ω) as shown in Fig. 4C. The small R_{ct} value of the Cs-MnO_x-450 reflected a high electron transfer rate as shown by the values of exchange current density and standard rate constant (Tables 2, and S2). At 10 mA/cm², LSV of the best optimized Cs-MnO_x catalyst (Cs-MnO_x-450) showed 50 and 60 mV more positive potential compared to Ir/C and RuO₂ catalysts respectively. However, at a high current density (> 26 mA/cm²), Cs-MnO_x-450 outperformed both Ir/C and RuO₂ with less positive potential observed for Cs-MnO_x-450 (Fig. 4A).

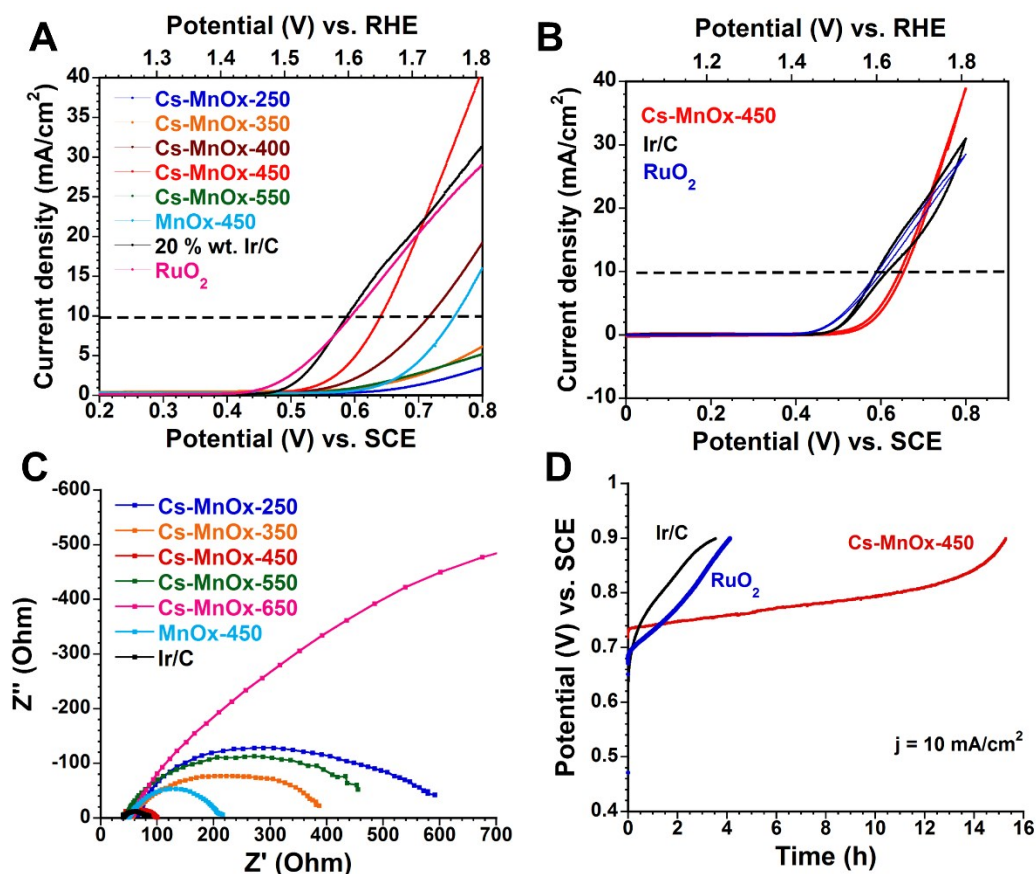


Fig. 4 Electrochemical characterization of OER in 0.1 M KOH. (A) LSV of different catalysts at a scan rate of 5 mV/s. (B) CVs of the highly active Cs-MnO_x-450 compared to Ir/C, and RuO₂ at scan rate of 5

mV/s. (C) EIS at potential of 0.7 V vs. SCE (1.71 V vs. RHE) and a frequency range of 0.1 to 10^5 Hz. (D) Chronopotentiometric curves (not iR compensated) at 10 mA/cm² showing superior stability of Cs-MnO_x-450 compared to Ir/C and RuO₂.

OER performance of Cs-MnO_x-450 was tested at extreme working potentials to study the change in the catalytic efficiency at extreme conditions. A nearly linear LSV curve was observed for potentials up to 1.7 V vs. SCE (2.71 V vs. RHE) achieving a very high current of 400 mA/cm² (**Fig. S4**), suggesting the capability of Cs-MnO_x-450 to work at low and high working potentials with reasonable efficiency. Tafel slopes of Cs-MnO_x-450 and Ir/C were also compared at low and high potential regions. In the low potential region, Cs-MnO_x-450 showed a Tafel slope of 100 mV/dec that is higher than that of Ir/C (80 mV/dec). However, Cs-MnO_x-450 displayed a smaller Tafel slope at high potentials as compared to Ir/C suggesting faster oxygen evolution reaction rate for the Cs-MnO_x-450 at high potentials (**Fig. S5**). Moreover, CV curves of the Cs-MnO_x showed well-defined and sharp CV curves with both anodic and cathodic curves nearly superimposed on one another (**Fig. 4B**). The stability was tested using chronopotentiometry at 10 mA/cm² with a maximum potential limit of 0.9 V vs. SCE (1.91 V vs. RHE) (**Fig. 4D**). The Cs-MnO_x-450 spent 15 h before the potential was shifted to 0.9 V vs. SCE which is almost four times higher stability compared to Ir/C and RuO₂. Moreover, Cs-MnO_x-450 showed much higher activity and stability compared to other forms of manganese oxides we have recently reported.²¹ The superior activity of the Cs-MnO_x-450 over Ir/C, RuO₂, and commercial Mn₂O₃ along with the high stability suggest that Cs ion promoted mesoporous manganese oxide is a strong candidate for water electrolyzers as well as fuel cells.

To gain full assessment about the properties of the catalyst in the oxygen evolution reaction, we determined Faradaic efficiency of Cs-MnO_x catalysts using a completely sealed H-shaped electrochemical cell in a three electrode configuration. The Pt counter electrode was positioned in the left arm of the cell, while the Ag/AgCl reference, working electrode, and the oxygen sensor were placed on the right arm. The cell was

filled with 0.1 M KOH as electrolyte and purged for 30 min with purified nitrogen before running the experiment.

An amperometric (current-time) experiment was performed with an input potential of 0.8 V vs. SCE for 3 min reaching a current of 106 mA. The theoretical number of moles of oxygen evolved can be calculated from Faraday's 2nd law of electrolysis according to the following equation:

$$n_{O_2}(\text{theoretical}) = \frac{Q}{nF} = \frac{i \times t}{nF} = \frac{0.106 \text{ (A)} \times 180 \text{ (s)}}{4 \times 96485.3 \text{ s A mol}^{-1}} = 49.4 \times 10^{-6} \text{ mole} \quad (1)$$

where n_{O_2} is the number of moles of oxygen produced, Q is the total charge passed during electrolysis, n is the number of electrons transferred during OER (4 e), i is the applied current in amps, t is the electrolysis time in sec, and F is the Faraday constant $96485.3 \text{ s A mol}^{-1}$.

The oxygen sensor detected the total number of moles of oxygen produced to be 45.2×10^{-6} moles.

$$\text{The faradic efficiency is} = \frac{n_{O_2}(\text{experimental})}{n_{O_2}(\text{theoretical})} \times 100 = 91.4 \% \quad (2)$$

These results verify that the current of the working electrode is exclusively caused by the oxygen evolution reaction.

Table 2: Summary for the OER electrocatalytic performance for the studied catalysts

Sample ID	E_j (V) @ 10 mA/cm ² ^a	R_{ct} (Ω) ^b	k^o (cm s ⁻¹) ^c	$\Delta E_{(OER-ORR)}$ (V) ^d
Cs-MnOx-250	0.90 (1.91)	412	0.0008	1.33
Cs-MnOx-350	0.86 (1.87)	256	0.0013	1.35
Cs-MnOx-450	0.64 (1.65)	50	0.0067	0.78
Cs-MnOx-550	0.90 (1.91)	360	0.0009	1.33
Cs-MnOx-650	> 1.09 (2.10)	1450	0.0002	> 1.42
MnOx-450	0.71 (1.72)	137	0.0025	1.08
20 % wt. Pt/C	1.0 (2.01)	N/A	N/A	1.17
20 % wt. Ir/C	0.58 (1.59)	37	0.0091	0.96
RuO ₂	0.59 (1.6)	N/A	N/A	N/A

All data in the tables are extracted from the LSV and EIS experiments in 0.1 M KOH at a rotation speed of 1600 rpm. ^a Potentials measured from LSV at a current density of 10 mA/cm², potentials are recorded in volts versus SCE, and converted to RHE in parentheses. ^b The charge transfer resistance (R_{ct}) obtained from EIS analysis at 0.7 V vs SCE. (1.71 V vs. RHE). ^c The standard rate constant as calculated from R_{ct} values. ^d The potential difference between OER at 10 mA/cm² and ORR at -3 mA/cm².

XANES and EXAFS analysis

To study the role of the Mn oxidation state for enhancing ORR and OER activity, X-ray absorption near edge structure (XANES) was used for the precise monitoring of the change in the average Mn oxidation state of the Cs-MnOx calcined at different temperatures. **Fig. 5A** shows the *Ex-situ* XANES spectra of Cs-MnOx calcined at 250 °C to 550 °C. **Fig. 5A** showed shift of the XANES spectra to higher energy upon increasing calcination temperature from 250 °C to 400 °C indicating an increase in the average Mn oxidation state, followed by a shift to lower energy when the calcination temperature further increased to 450 °C or 550 °C indicating a subsequent decrease in Mn oxidation state. Different manganese oxides with variable oxidation states of Mn (MnO, Mn₃O₄, Mn₂O₃, MnO₂) were used as standards for the linear combination fitting (LCF) of the XANES spectra of the Cs-MnOx calcined at different temperatures to monitor the contribution of the different manganese oxide phases and track the change of the oxidation state as well upon calcination (**Fig. 5B and S6**). **Fig. 5B** showed the LCF results of the XANES spectra revealing the contribution of each Mn oxidation state at each calcination temperature. LCF results showed that all samples calcined to a temperature below 450 °C have mixed Mn valence, while transformation to pure bixbyite phase occur at 450 °C and 550°C. **Fig. 5C** shows the change of the average Mn oxidation state from 2.97 to 3.34 when the calcination temperature increases from 250 °C to 400 °C, then the Mn oxidation state dropped back to 3.00 when the calcination temperature increases to 450 °C or 550 °C (**Fig. 5C**). The trend observed in the XANES analysis upon conversion from 350 °C to 550 °C was confirmed by the EXAFS analysis (**Fig. 5D and S7**). Whereas Samples calcined at 450 °C and 550 °C show quite similar Fourier transform EXAFS spectra to standard Mn₂O₃, while 350 °C shows significantly different FT EXAFS spectra (**Fig. S8**) with shorter Mn-Mn bond length (**Table S3**). Furthermore, the effect of applying constant potentials for ORR (-0.3 V vs. SCE for 5 h) and OER (0.7 V vs. SCE for 1 h) on the oxidation state of Mn in the best optimized Cs-MnOx-450 was investigated using XANES analysis (**Fig. 6**). Results showed that exposing Cs-MnOx-450 to either ORR or OER induced changes in the valence of Mn centers of the catalyst. After exposing Cs-MnOx-450 to ORR for 5 hours, the average oxidation state of Mn shows

no significant change (from 3.00 to 3.02). However, the contribution of the different Mn oxidation states to the average oxidation state showed significant changes with dropping of the percentage of Mn^{3+} from 100 % to 71 %, as well as increasing the percentage of Mn^{4+} from 0.0 to 9.0 %. In case of exposing Cs-MnOx-450 to OER for 1 h, the average oxidation state increased from 3.00 to 3.17 where percentage of Mn^{4+} increased from 0 to 23 % along with decrease in the percentage of Mn^{3+} to 57 % (**Fig. 6**).

Discussion

The structures and surface area of metal oxides are believed to be main decisive factors in the ORR and OER catalysis as structural flexibility and surface accessibility are important degrees of freedom. For the rational design of highly active ORR and OER metal oxide catalysts, it is often difficult to choose crystalline phase or amorphous phase as the active form of catalyst.^{12, 32, 33} In our study, we were able to tune high surface area mesoporous manganese oxide from amorphous phase to crystalline one by mere heat treatment for developing exceptionally active manganese oxide catalysts. Our materials, unlike conventional mesoporous materials, have a connection of intraparticle voids of closely packed manganese oxide nanocrystals that form the mesoporous structure.^{28, 29} Amorphous Cs-MnOx materials calcined at 250 °C and 350 °C showed much lower catalytic activity (in terms of current and onset potential) for ORR and OER than crystalline Cs-MnOx calcined at 450 °C (bixbyite phase). Interestingly, the surface area of the amorphous Cs-MnOx-350 (106 m²/g) is 23 % higher than crystalline Cs-MnOx-450 (86 m²/g), yet the activity of Cs-MnOx-450 for ORR and OER is much higher, indicating that the effect of crystallinity is masking the effect of surface area. The Cs-MnOx calcined at 550 °C also possessed the bixbyite (Mn_2O_3) phase with 38 % lower surface area than Cs-MnOx-450 explaining the drop in the ORR and OER activity upon increasing the calcination temperature from 450 °C to 550 °C. On the other hand, the much lower surface area of both Cs-MnOx-650 (13 m²/g) and commercial Mn_2O_3 (12 m²/g), explains the relatively inert behavior under electrochemical conditions. Furthermore, we verified the performance of Cs-MnOx-450 and commercial Mn_2O_3 in OER by normalizing the current to the true surface area. Figure S9 revealed that the Cs-MnOx-450 showed higher current density than commercial Mn_2O_3 even after normalizing the

surface area. These results suggest that the combination of high surface area and crystalline structure are determining factors behind the superior performance of Cs-MnOx-450 as an electrocatalyst. In order to confirm the influence of specific surface area on the electrochemical behavior, we investigated the electrochemically active surface area (ECSA) of Cs-MnOx at different calcination temperatures (determined from the capacitance). Cs-MnOx-250 showed a capacitance of 22 mF/cm² that almost doubled when the calcination temperature increased to 350 °C (41 mF/cm²) indicating an increase in the accessible electrochemical active surface area to the electrolyte (**Fig. S10, Table S4**). The capacitance was then dropped to 20 mF/cm² when the calcination temperature increased to 450 °C, followed by further decrease in the capacitance at 550 °C (13 mF/cm²). The change of the ECSA is in great agreement with findings from BET. However, ECSA has much lower values than the surface area determined by BET (See SI for more details) because of the limited access of the electrolyte to the pores of the catalyst compared with the inert gas used for BET.

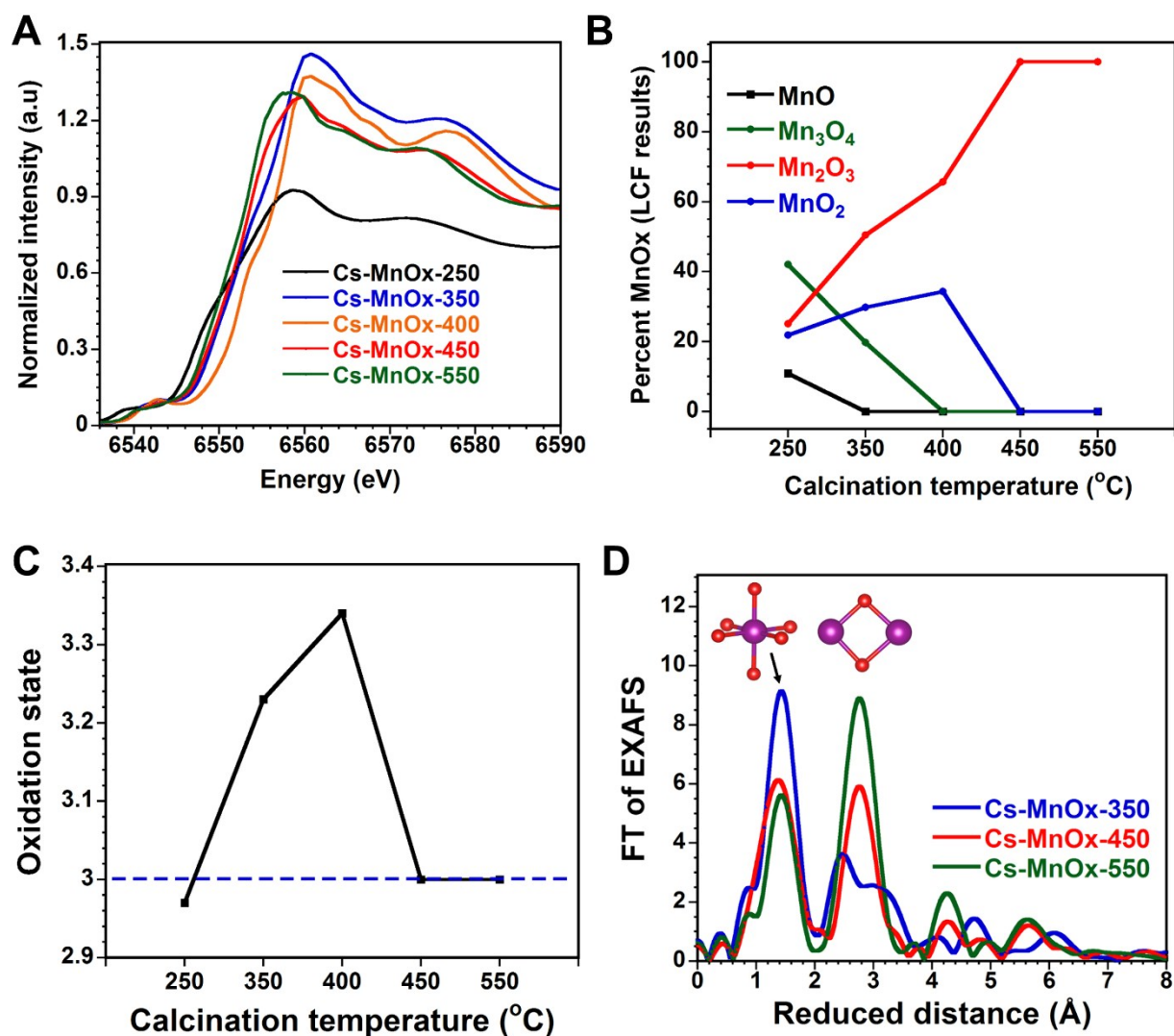


Fig. 5 Ex-situ XANES and EXAFS study for Cs-MnOx catalysts. (A) Normalized Mn K edge XANES spectra. (B) Linear combinations fits of data in A. (C) Corresponding change of Mn oxidation state obtained from XANES analysis via linear combination fitting. (D) Ex-situ EXAFS of Cs-MnOx samples calcined at 350 °C - 550 °C showing change in EXAFS spectra upon conversion from amorphous (350 °C) to bixbyite phase (450 °C and 550 °C).

Oxidation state of active manganese centers is critical for designing active ORR and OER manganese oxide catalysts. The success of catalytic activity in ORR and OER largely depends on the role of the Mn³⁺ oxidation state as the intermediate species for these reactions.^{34, 35} Several strategies have been

adopted to generate the active Mn^{3+} species irrespective of the initial oxidation state of Mn to enhance the catalytic activity.^{26, 36} The high catalytic activity of the Mn^{3+} species is attributed to the presence of one electron in the antibonding e_g orbital (e_g^1) which result in Jahn-Teller (J-T) distorted metal-oxygen octahedra. Moreover, the presence of single electron in the e_g^1 results in the appropriate interaction between O_2 and the manganese oxide catalyst required for efficient ORR and OER.³⁷ Linear combination fitting of the XANES spectra revealed the contribution of Mn^{3+} to the catalytic ORR and OER activity. However, though the average oxidation state of Mn in Cs-MnOx-250 is ~ 3.00 (exactly 2.97), the ORR and OER activities are relatively low as the result of the mixed Mn valence with only 25 % of Mn ions in the form of Mn^{3+} (**Fig. 5**). Slight enhancement in ORR and OER activity was observed as the percentage of Mn^{3+} increases when the calcination temperature increases to 350 °C. The highest ORR and OER activity among all calcination temperatures was achieved only when the contribution of Mn^{3+} reached 100 % in case of Cs-MnOx-450. XANES analysis was further used to monitor the effect of exposing Cs-MnOx-450 to ORR and OER reactions to explain the slight decrease in stability overtime (**Fig. 6**). LCF of XANES results revealed that exposure to ORR and OER induced a change in the contribution of different Mn oxidation state with dropping in the percentage of Mn^{3+} (**Fig. 6**). These results suggest that an average Mn oxidation state of 3 alone does not produce active ORR and OER manganese oxide catalyst, but rather higher percentage of Mn^{3+} in the form of bixbyite phase is the main reason behind superior ORR and OER activity in manganese oxide.

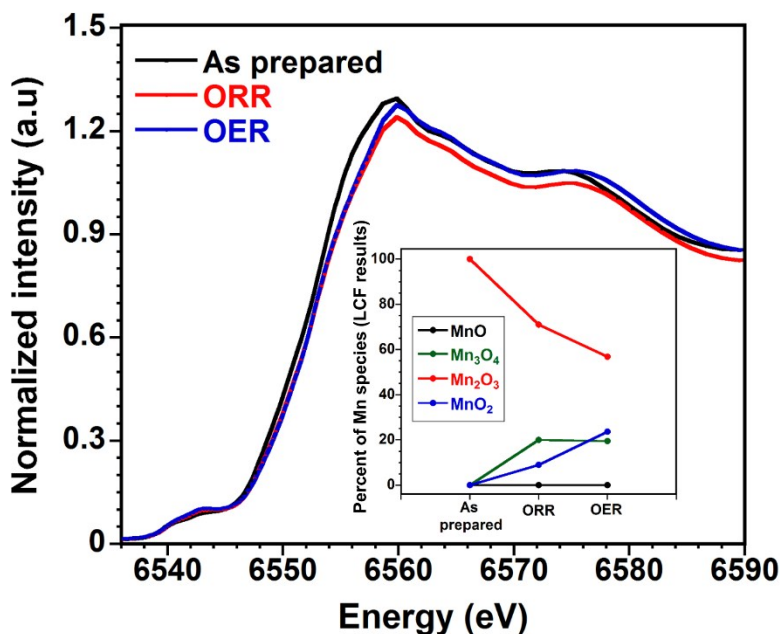


Fig. 6 Normalized Mn K edge XANES spectra for the as prepared Cs-MnOx-450, after exposure to ORR for 5 h at -0.3 V vs. SCE, and after exposure to OER for 1 h at 0.7 V vs. SCE. The average Mn oxidation state changed from 3.00 to 3.02 in case of ORR, and to 3.17 in case of OER.

The role of Cs in altering the bulk and surface properties of Cs-MnOx material compared to nonpromoted MnOx material was investigated to understand the origin of the high ORR and OER activity of the Cs-MnOx material. Temperature resolved powder X-ray diffraction (TR-PXRD) was performed on Cs-MnOx and MnOx (calcined at 250 °C) to investigate the phase transformation with heat treatment (**Fig. S11 and S12**). Both of the materials are amorphous at room temperature. A clear difference can be seen in the crystallinity of the materials with and without the introduction of Cs ions. In the nonpromoted sample, the amorphous state crystallizes first to the vernadite (MnOOH) phase before undergoing rearrangement to the bixbyite (Mn₂O₃) phase (**Fig. S11**). The addition of Cs ions resulted in the destabilization of vernadite phase and presenting bixbyite phase with no intermediary phase (**Fig. S12**). The amorphous state of the material was stable > 350 °C for Cs-MnOx (crystallized at 400°C), whereas, MnOx crystallized at 350°C. Thermogravimetric analysis (TGA) (**Fig. S13**) supports the destabilizing effect due to Cs introduction by showing a full 15 % increase in mass loss which was ascribed to labile oxygen in the amorphous phase

compared with MnO_x, which exhibited a higher thermal stability and by extension, less labile oxygen. The nonpromoted MnO_x displayed the presence of both active Mn³⁺ along with less active Mn⁴⁺ species (80/20 ratio) as determined by the deconvoluted Mn2p_{3/2} XPS spectra (**Fig. S14**). The presence of Cs stabilized the active Mn³⁺ species with no other Mn oxidation states. These results indicate that the presence of surface active Mn³⁺ species and stabilization of active crystal phase (Mn₂O₃) are the main reasons of the superior ORR and OER activity of Cs-MnO_x over MnO_x. The strong adsorption of protons (due to the OH⁻ dissociation) is one of the important factors for a facile OER catalyst in alkaline medium.²¹ The remarkable activity of the Cs promoted material over the non-promoted material can be also be ascribed to the increase of relative basicity of the materials. The CO₂ chemisorption measurements revealed the more basic nature of Cs-MnO_x over MnO_x at three different probe temperatures (**Fig. S15**). The acidic CO₂ adsorbed more into the basic material, which is in line with our previous work, where the basic nature of Cs-MnO_x was the reason for superior chemical oxidation and esterification catalysis.²⁷

To further study the role of surface and bulk manganese centers in relation to activity, ab-initio models for three bulk oxides of manganese (MnO, Mn₂O₃ and MnO₂) were optimized using density functional theory (DFT), and their experimentally relevant surface terminations, [200], [222] and [110], respectively, were generated to model the thermodynamics of ORR and OER reaction as two reversible processes (**Fig. 7**). The overall reaction of ORR in a four electron transfer process is shown in Eqn. 3:



The ORR mechanism catalyzed by manganese oxide can be expressed as:^{24, 38}



Table 3: Bader charge analysis of MnO_x in the bulk and surfaces

Location	MnO	Mn ₂ O ₃	MnO ₂
Surface	1.32	1.61	1.71
Bulk	1.42	1.73	1.83

The thermodynamic reaction pathway for the dissociation of water was meticulously analyzed (**Fig. 7B, S16, and Table S4, S5**). The overall reaction pathway illustrated that MnO₂ surfaces have the lowest ΔH between consecutive steps, and often the lower the ΔH between consecutive steps the lower its associated E_a , based on the guidelines of Sabatier's principle. Given these three surface terminations, the thermodynamic preference is: MnO₂ > Mn₂O₃ > MnO suggesting that MnO₂ surfaces would require the least reduction potential.

However, terminating a surface reduces its coordination.³⁹ To identify the active oxidation states on the Mn surfaces, a Bader charge analysis⁴⁰⁻⁴² was conducted on Mn ions in their corresponding bulk phase and on the surface. **Table 3** summarizes the observed charges at the two locations. Mn ions on the MnO₂ surface have an identical charge to Mn ions in bulk Mn₂O₃ which are known to be in the +3 oxidation state. This observation along with the favored thermodynamic activity behavior on the MnO₂ surface suggests that Mn³⁺ ions are contributing positively to an enhanced ORR/OER activity. Moreover, the change in the charge between the surface and bulk of the same oxide suggested the necessity of tuning the surface of metal oxides to achieve the active oxidation state for ORR and OER as presented in our current study as the role of Cs.

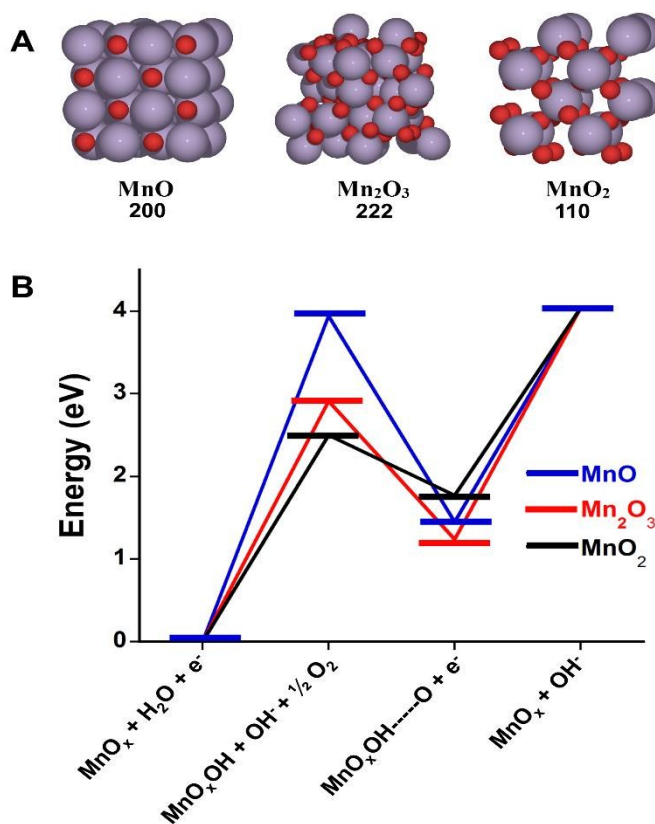


Fig. 7 (A) Bulk structure of MnO, Mn₂O₃ and MnO₂ with their relevant experimental surface terminations. Purple atoms are Mn and red atoms are O. (B) Elementary reaction pathway for the dissociation of H₂O on MnO_x terminated surfaces.

Conclusion

In summary, we have successfully tuned mesoporous manganese oxide from amorphous to crystalline phase along with exploring the role of surface and bulk active manganese centers to achieve exceptional ORR and OER activities. The crystalline phase of our mesoporous manganese oxide material outperformed the amorphous phase for both ORR and OER. Findings from XANES, EXAFS, XPS, PXRD, and DFT calculations revealed the critical role of the surface and bulk active Mn³⁺ for enhancing the catalytic activity for ORR and OER. By incorporating a minute amount of electropositive Cs ions (0.16 %), surface enriched Mn³⁺ was achieved, and the catalytic activity in both ORR and OER was significantly enhanced compared to pure mesoporous manganese oxide (5 times faster reaction rate in ORR and 7 orders higher turnover

frequency in OER). Moreover, the best optimized Cs-MnOx-450 material exhibited better bifunctional oxygen reaction activity than precious metal catalysts: Pt (in ORR) and Ir, Ru (in OER at high current density) and other noble metal free manganese based catalysts reported to date (Table S6, S7). Precise control over the structural and surface properties by simple heat treatment made Cs-MnOx a ubiquitous electrocatalyst and opens up new avenues in the field of alternate energy applications in terms of non-expensive and earth-abundant metal oxides.

Experimental section

Catalyst Synthesis

Synthesis of Cs-MnOx: The synthesis followed our recent published article.¹⁹ In a typical synthesis manganese nitrate tetrahydrate ($\text{Mn}(\text{NO}_3)_2 \cdot 4\text{H}_2\text{O}$, 0.02 mol) and 1-butanol (0.134 mol) were added into a 120 mL beaker. To this solution Poly(ethylene glycol)-*block*-poly(propylene glycol)-*block*-poly(ethylene glycol) (0.0034 mol) (Pluoronic P123, $\text{PEO}_{20}\text{PPO}_{70}\text{PEO}_{20}$, molar mass 5750 g mol^{-1}) and concentrated nitric acid (0.032 mol) (HNO_3) were added and stirred at room temperature until the solution became clear (light pink). To this clear solution 200 μL of 1.0M CsNO_3 was added maintaining the Mn/Cs ratio 100/1, mol/mol. The resulting clear solution was then kept in an oven at 120 °C for 3 h under air. The black material was washed with excess ethanol, centrifuged, and dried in a vacuum oven overnight. The dried black powders were subjected to a heating cycle. First they were heated at 150 °C for 12 h and cooled down to room temperature under ambient conditions followed by heating steps of 250 °C for 3 h, 350 °C for 2 h, 450 °C for 1 h, 550 °C for 1h, and 650 °C for 1 h.

Synthesis of MnOx: Synthesis of the non-promoted MnOx followed the same procedure of the Cs-MnOx, but without addition of any Cs precursor.

* It is recommended to perform all reactions in ovens with proper ventilation due to release of toxic NOx from the gel during the reaction.

Electrochemical Characterization:

Electrocatalytic performance of all studied catalysts towards oxygen reduction reaction (ORR), and oxygen evolution reaction (OER) was characterized on three electrode electrochemical cell connected to CHI 660A electrochemical workstation. Cyclic voltammetry (CV), linear sweep voltammetry (LSV), electrochemical impedance spectroscopy (EIS), chronopotentiometry, and chronoamperometry were performed in 0.1 M KOH purged with high purity oxygen or argon for 30 min before start running the electrochemical measurement, with flowing the gas over the solution surface during the data collection. Standard calomel electrode (SCE) was used as reference electrode, while pyrolytic graphite was used as both working and counter electrodes.

Electrode preparation:

Pyrolytic graphite (PG) electrode was polished using silicon carbide grinding paper before sonicating in ethanol and water (2 min each) to produce clean, and smooth PG surface. The catalyst ink was prepared by mixing 4 mg of catalyst, 1 mg of carbon black, and 85 μL Nafion in 1.0 mL of DI water/ethanol mixture (4:1). The catalyst ink was sonicated for 5 min to ensure proper mixing of the component, and then loaded to the rotating disc PG electrode (mass loading 0.28 mg/cm^2) by controlled drop casting method. The catalyst ink was incubated on the PG surface overnight in room temperature before running electrochemical measurements.

Calculations:

Koutecky-Levich (K-L) plots were studied to interpret the ORR results. The number of electron transferred per one oxygen molecule (n) can be obtained from K-L plots by applying the following equations:

$$\frac{1}{J} = \frac{1}{J_L} + \frac{1}{J_K} = \frac{1}{B\omega^{1/2}} + \frac{1}{J_K}$$

$$B = 0.62nFC_O(D_O)^{2/3}\nu^{-1/6}$$

$$J_k = nFKC_O$$

Where, J is the measured current density, J_k is the kinetic current, J_L is the diffusion limiting current, ω is the rotation speed of the electrode in rad s^{-1} , B is the reciprocal of the slope of the K-L plots, F is Faraday constant (96485 C mol^{-1}), C_O is the saturated concentration of oxygen in 0.1 M KOH ($1.2 \times 10^{-6} \text{ mol cm}^{-3}$), D_O is the diffusion coefficient of O_2 ($1.9 \times 10^{-5} \text{ cm}^2 \text{ s}^{-1}$), ν is kinematic viscosity of the electrolyte ($0.01 \text{ cm}^2 \text{ s}^{-1}$), k is electron transfer rate constant for the ORR.

Calculation of mass activity and turn over frequency (TOF):

$$\text{Mass Activity} = \frac{j}{M}$$

Where j is the current density in A/cm^2 , while M is the mass of the loaded catalyst in grams. TOF (s^{-1}) was calculated according to the following formula:

$$\text{TOF} = \frac{jA}{4nF}$$

Where j is the current density (A/cm^2), A is working electrode surface area (cm^2), n is the number of moles of the loaded catalyst onto the working electrode, and F is the Faraday constant (C mol^{-1}).

Calculations of standard rate constant (k^0)

Using the charge transfer resistance (R_{ct}) obtained from the EIS data, k^0 was calculated using the following formulas:

$$J_0 = \frac{i_0}{A} = \frac{RT}{nAF R_{ct}}$$

$$k^0 = \frac{i_0}{nFC}$$

Where J_0 is the exchange current density, i_0 is the exchange current, A is the electrode surface area, R is the gas constant, T is the absolute temperature, n is the number of electrons transferred (assumed to be 4 in both ORR and OER for all catalyst for comparison), F is Faraday's constant, C is the saturated concentration of oxygen in 0.1 M KOH.

Acknowledgements

SLS acknowledges the support of the US Department of Energy, Basic Energy Sciences, Division of Chemical, Geological and Biological Science under grant DE-FG02-86ER13622.A000.

References

1. S. Chu and A. Majumdar, *Nature*, 2012, **488**, 294-303.
2. N. S. Lewis and D. G. Nocera, *Proc. Natl. Acad. Sci.*, 2006, **103**, 15729-15735.
3. T. E. Mallouk, *Nat. Chem.*, 2013, **5**, 362-363.
4. J. Suntivich, H. A. Gasteiger, N. Yabuuchi, H. Nakanishi, J. B. Goodenough and Y. Shao-Horn, *Nat. Chem.*, 2011, **3**, 546-550.
5. J. Zhang, Y. Zhao, X. Zhao, Z. Liu and W. Chen, *Sci. Rep.*, 2014, **4**.
6. X. Huang, Z. Zhao, L. Cao, Y. Chen, E. Zhu, Z. Lin, M. Li, A. Yan, A. Zettl, Y. M. Wang, X. Duan, T. Mueller and Y. Huang, *Science*, 2015, **348**, 1230-1234.
7. Y. Lee, J. Suntivich, K. J. May, E. E. Perry and Y. Shao-Horn, *J. Phys. Chem. Lett.*, 2012, **3**, 399-404.
8. M. Lefèvre, E. Proietti, F. Jaouen and J.-P. Dodelet, *Science*, 2009, **324**, 71-74.
9. Y. Liang, H. Wang, J. Zhou, Y. Li, J. Wang, T. Regier and H. Dai, *J. Am. Chem. Soc.*, 2012, **134**, 3517-3523.
10. J. Masa, W. Xia, I. Sinev, A. Zhao, Z. Sun, S. Grutzke, P. Weide, M. Muhler and W. Schuhmann, *Angew. Chem. Int. Ed. Engl.*, 2014, **53**, 8508-8512.
11. S. L. Suib, *Acc. chem. res.*, 2008, **41**, 479-487.
12. C.-H. Kuo, I. Mosa, A. S. S. Poyraz, S. Biswas, A. M. El-Sawy, W. Song, Z. Luo, S.-Y. Chen, J. F. Rusling, J. He and S. L. Suib, *ACS Catal.*, 2015, **5**, 1693-1699.
13. G. C. Dismukes, R. Brimblecombe, G. A. Felton, R. S. Pryadun, J. E. Sheats, L. Spiccia and G. F. Swiegers, *Acc. chem. res.*, 2009, **42**, 1935-1943.
14. K. N. Ferreira, T. M. Iverson, K. Maghlaoui, J. Barber and S. Iwata, *Science*, 2004, **303**, 1831-1838.
15. A. M. El-Sawy, C. K. King'ondou, C.-H. Kuo, D. A. Kriz, C. J. Guild, Y. Meng, S. J. Frueh, S. Dharmarathna, S. N. Ehrlich and S. L. Suib, *Chem. Mater.*, 2014, **26**, 5752-5760.
16. A. Indra, P. W. Menezes, I. Zaharieva, E. Baktash, J. Pfrommer, M. Schwarze, H. Dau and M. Driess, *Angew. Chem. Int. Ed.*, 2013, **52**, 13206-13210.
17. H.-Y. Su, Y. Gorlin, I. C. Man, F. Calle-Vallejo, J. K. Norskov, T. F. Jaramillo and J. Rossmeisl, *Phys. Chem. Chem. Phys.*, 2012, **14**, 14010-14022.

18. F. Zhou, A. Izgorodin, R. K. Hocking, L. Spiccia and D. R. MacFarlane, *Adv. Energy Mater.*, 2012, **2**, 1013-1021.
19. C.-H. Kuo, I. M. Mosa, S. Thanneeru, V. Sharma, L. Zhang, S. Biswas, M. Aindow, S. Pamir Alpay, J. F. Rusling, S. L. Suib and J. He, *Chem. Commun.*, 2015, **51**, 5951-5954.
20. Y. Gorlin, B. Lassalle-Kaiser, J. D. Benck, S. Gul, S. M. Webb, V. K. Yachandra, J. Yano and T. F. Jaramillo, *J. Am. Chem. Soc.*, 2013, **135**, 8525-8534.
21. Y. Meng, W. Song, H. Huang, Z. Ren, S. Y. Chen and S. L. Suib, *J. Am. Chem. Soc.*, 2014, **136**, 11452-11464.
22. U. Ciesla and F. Schüth, *Micropor. Mesopor. Mater.*, 1999, **27**, 131-149.
23. C. T. Kresge, M. E. Leonowicz, W. J. Roth, J. C. Vartuli and J. S. Beck, *Nature*, 1992, **359**, 710-712.
24. R. Liu, D. Wu, X. Feng and K. Müllen, *Angew. Chem.*, 2010, **122**, 2619-2623.
25. Y. Gorlin, C.-J. Chung, J. D. Benck, D. Nordlund, L. Seitz, T.-C. Weng, D. Sokaras, B. M. Clemens and T. F. Jaramillo, *J. Am. Chem. Soc.*, 2014, **136**, 4920-4926.
26. C.-H. Kuo, W. Li, L. Pahalagedara, A. M. El-Sawy, D. Kriz, N. Genz, C. Guild, T. Ressler, S. L. Suib and J. He, *Angew. Chem. Intern. Ed.*, 2015, **54**, 2345-2350.
27. M. Wiechen, I. Zaharieva, H. Dau and P. Kurz, *Chem. Sci.*, 2012, **3**, 2330-2339.
28. S. Biswas, A. S. Poyraz, Y. Meng, C.-H. Kuo, C. Guild, H. Tripp and S. L. Suib, *Appl. Catal. B: Environ.*, 2015, **165**, 731-741.
29. A. S. Poyraz, C.-H. Kuo, S. Biswas, C. K. King'ondou and S. L. Suib, *Nat. Commun.*, 2013, **4**, 2952.
30. X. Wang, M. Waje and Y. Yan, *J. Electrochem. Soc.*, 2004, **151**, A2183-A2188.
31. K. Kamiya, R. Kamai, K. Hashimoto and S. Nakanishi, *Nat. Commun.*, 2014, **5**, 5040.
32. A. Indra, P. W. Menezes, N. R. Sahraie, A. Bergmann, C. Das, M. Tallarida, D. Schmeisser, P. Strasser and M. Driess, *J. Am. Chem. Soc.*, 2014, **136**, 17530-17536.
33. A. Iyer, J. Del-Pilar, C. K. King'ondou, E. Kissel, H. F. Garces, H. Huang, A. M. El-Sawy, P. K. Dutta and S. L. Suib, *J. Phys. Chem. C*, 2012, **116**, 6474-6483.
34. Y. Gorlin and T. F. Jaramillo, *J. Am. Chem. Soc.*, 2010, **132**, 13612-13614.
35. Derrick R. J. Kolling, N. Cox, Gennady M. Ananyev, Ron J. Pace and G. C. Dismukes, *Biophys. J.*, 2012, **103**, 313-322.
36. K. Jin, A. Chu, J. Park, D. Jeong, S. E. Jerng, U. Sim, H.-Y. Jeong, C. W. Lee, Y.-S. Park, K. D. Yang, G. Kumar Pradhan, D. Kim, N.-E. Sung, S. Hee Kim and K. T. Nam, *Sci. Rep.*, 2015, **5**.
37. U. Maitra, B. S. Naidu, A. Govindaraj and C. N. Rao, *Proc. Natl. Acad. Sci.*, 2013, **110**, 11704-11707.
38. I. Roche, E. Chaînet, M. Chatenet and J. Vondrák, *J. Phys. Chem. C*, 2006, **111**, 1434-1443.
39. V. Botu, R. Ramprasad and A. B. Mhadeshwar, *Surf. Sci.*, 2014, **619**, 49-58.
40. G. Henkelman, A. Arnaldsson and H. Jónsson, *Comput. Mater. Sci.*, 2006, **36**, 354-360.
41. E. Sanville, S. D. Kenny, R. Smith and G. Henkelman, *J. comput. Chem.*, 2007, **28**, 899-908.
42. W. Tang, E. Sanville and G. Henkelman, *J. Phys-Condens. Mat.*, 2009, **21**, 084204.

